*Assessing the influence of atmospheric and topographic correction and inclusion of SWIR bands in burned scars detection from high-resolution EO imagery*

Abbi Said, Yahia; Petropoulos, George; Srivastava, Prashant K.

# Assessing the Influence of Atmospheric, Topographic Correction and SWIR bands Inclusion in Burnt Scars Detection from High Resolution EO Imagery: A Case Study Using ASTER

Yahia Abbi Said[1], George P. Petropoulos[2,*], Prashant K. Srivastava[3,4]

[1]*Mediterranean Agronomic Institute of Chania, Chania 73100, Crete, Greece*
[2]*Department of Geography & Earth Sciences, University of Aberystwyth, SY23 2DB, United Kingdom*
[3]*Earth System Science Interdisciplinary Center, University of Maryland, Maryland, USA*
[4]*NASA Goddard Space Flight Center, Greenbelt, Maryland, USA*

* *Correspondence to: [george.petropoulos@aber.ac.uk](mailto:george.petropoulos@aber.ac.uk), Tel: +44-0-1970-621861*

## Abstract

In the present study the effect of atmospheric and topographic correction to the burnt area delineation from EO imagery in conditions characteristic of a Mediterranean environment is explored. Furthermore, the potential added-value of the inclusion of the shortwave infrared (SWIR) bands in improving the retrievals of burned area cartography is investigated. In particular the capability of ASTER imagery when combined with the Maximum Likelihood (ML) and the Support Vector Machines (SVMs) classification techniques has been examined herein. As a case study a Mediterranean site on which a fire event occurred in Greece during 2007, for which post-fire ASTER imagery has been available is used. The combination of topographic correction (orthorectification) with the inclusion of the SWIR bands returned the most accurate results in burnt area detection. SVMs showed the highest accuracy, showing the most promising potential in delineating the burned areas. The most accurate results for burnt scar mapping were obtained from the combined use of SVMs with an orthorectified image and SWIR spectral bands, at least this appeared to be the case in our study site.

Our results offer a very important contribution to the understanding of the capability of high resolution imagery such as that from ASTER in burnt area estimation. Also, corroborate the usefulness particularly of the topographic correction as an image processing step to be incorporated in modeling schemes for delineating burnt areas from such data. Findings provide potentially very useful information towards the development of EO-based techniques that aim to operationally provide services related to the estimation of burnt area. This is of considerable scientific and practical value to the wider scientific and users' community given the continuation of free access today to observations from space from high resolution sensors globally.

**Keywords**: *burnt area mapping, ASTER, topography, atmospheric correction, remote sensing, wildfires, Greece*

## 1. Introduction

Wildfires are a powerful management tool in some ecosystems, used long term or short term to change the landscape and floristic components of ecosystems (Salvador *et al.*, 2005). Yet, they are also considered as of the most widespread disturbances of Earth's natural system. Those are affecting the land component of the Earth system by causing dramatic changes to land cover distribution and land surface processes dynamics at a variety of spatial and temporal scales of natural ecosystems (Koutsias et al., 2011; Petropoulos *et al.*, 2012b; Cawson et al., 2013). Moreover, they deteriorate habitat, diminishing biodiversity (Cao *et al.*, 2009), plant reproduction (Johnstone *et al.*, 2004) and nutrients cycling (Cao *et al.*, 2009). Wildfires also affect the Earth's land surface energy and water cycle, decreasing evapotranspiration and increasing surface albedo, surface runoff, erosion and sediment production (Pérez-Cabello *et al.*, 2006), resulting to triggering also phenomena such as floods and desertification. Thus, it is understandable why being able to acquire information on fire events has been underlined as a topic of key importance and priority for future attention by both scientists and policy makers (Boustras and Boukas, 2013; Kontoes *et al.*, 2013).

Being able to obtain accurate as well as rapid mapping of burnt areas in particular after a fire suppression, is of key importance in decision making, as it can be used effectively in establishing rehabilitation and restoration policies in the affected areas and also assisting to avoid post-fire hazards and long-term degradation (Vafeidis & Drake, 2005; Giglio *et al.,* 2009). Acquiring information on burnt area on a consistent monitoring basis can also provide important information on land cover changes related to ecology and biodiversity at different observational scales, which can significantly assist in understanding post-fire recovery of affected areas (Li *et al.,* 2004). An accurate cartography of the area burnt is important as the latter is also one of the key inputs in modelling the atmospheric and climatic impacts of biomass burning, and in estimating the total atmospheric emissions from it (Kasischke and French, 1995; Cao et al., 2009; Giglio et al., 2009; Petropoulos et al., 2010b).

Earth Observation (EO) technology has demonstrated promising potential in the mapping and analysis of wildfires (Ahern *et al.*, 2001; Chuvieco *et al.*, 2008). A major goal in satellite remote sensing of fire is to derive globally accurate measurements of the spatial and temporal distribution of burning (Fuller, 2000). Key advantages of EO technology include its ability to provide timely and often inexpensively spectral information at a variable spatial resolution from local, to regional and global scale ( Patel *et al.*, 2013). Particularly the integration of EO datasets with Geographic Information Systems (GIS) spatial analysis techniques provides an excellent framework for data capture, storage, synthesis and analysis of acquired spatial data related to wildfire analysis, including burnt area mapping. Different types of EO data have been exploited for more than 20 years now in performing various fire analysis investigations, including ones focusing on mapping the extent of burnt areas (Knorr et al., 2011; Petropoulos et al., 2010b). As a result, various related operational products have also been developed, currently distributed no-cost and at a wide range of spatial resolutions as regional or continental scale products (Schroeder *et al.*, 2008).

Satellite image classification consists perhaps the most widely used image analysis approach employed in deriving information on the pattern and the spatial distribution of burnt areas, particularly so from high to very high resolution EO datasets (Levin et al., 2012; Hope et

al., 2012, Huesca et al. 2013; ). Numerous classification techniques have been proposed and explored for this purpose (for a review see Lu and Weng, 2007). Maximum Likelihood (ML, Foody *et al.*, 1992) is a supervised pixel-based, parametric classification approach extensively used in deriving burnt area estimates from different sensors (Turner *et al.*, 1994). Support Vector Machines (SVMs, Vapnik *et al.*, 1997) is a relatively new machine learning-based non-parametric classifier. Its use so far has shown a promising potential in mapping changes to land cover from natural hazards including obtaining burnt areas cartography (Petropoulos *et al.*, 2011). Yet, despite their promising potential and their relative advantages over parametric classifiers (such as ML), their use still is being ill-explored in burnt area related studies in comparison to other classification approaches. Thus evidently, a comparative study of the performances of the different classifiers would be an interesting task to be performed. Indeed, performing studies assessing the performance of diverse, widely-used classifiers is an important step towards increasing the accuracy with which information on land use/cover and burnt areas can be derived from space (Lu and Weng, 2007). This is particularly interesting as well and in the development of algorithms suitable potentially for satellite sensors recently launched, such as Landsat 8, or due to be launched, such as the Sentinels 2 mission.

A review of the relevant literature also suggests that selection of the suitable classifier as well as of the appropriate spectral bands, original or derived, is crucial for improved classification accuracies, and consequently burnt area estimates (Stroppiana et al., 2003; Petropoulos et al., 2012c). Yet, aspects related to the inclusion of certain image processing steps such as of the atmospheric and topographic correction or of the shortwave infrared (SWIR) bands where available to our knowledge seem to have so far been ill-addressed (Bastarrika et al., 2011; Gitas and Devereux, 2006; Van Wagtendonk et al., 2004). This despite the significance of obtaining more accurately estimates of burnt areas, which might be of key importance to particular users. Also, given that burnt area estimates derived from high resolution EO imagery are often used as reference in validating burnt area operational products which are distributed globally (Justice et al., 2002; Roy and Boschetti, 2009; Simon et al., 2004; Tsela et al., 2014), it is understandable that this in turn could potentially help also in deriving more objectively information about the accuracy of currently distributed relevant operational products. Last but not least, if such studies were performed in regions like the Mediterranean basin can be very significant, given the high occurrence of fires in those areas and their relevance to other phenomena also taking place in those areas including land degradation and desertification (Castillejo-González et al., 2009).

Based on this context, this study aims at examining the effect of atmospheric and topographic correction image processing steps as key steps to be included to modelling the retrievals of burnt area mapping from Advanced Spaceborne Thermal Emission and Reflection Radiometer (ASTER) operationally distributed products globally when the latter is combined with the ML and the SVMs techniques. In addition, the potential added-value of the (SWIR) bands inclusion in improving burned area cartography from the acquired ASTER data is also explored. As a case study is selected a typical Mediterranean site in Greece, for which ASTER imagery acquired shortly after the fire suppression was available.

## 2. Study Area

Mt. Parnitha was selected the study site to satisfy the objectives of this work. It is located approximately 30 km north of the capital of Greece, Athens (Figure 1). The area covers approximately 200 km$^2$ of land with an altitude ranging from 200-1,400 m above sea level (a.s.l.). The region is covered mainly by Greek Fir (*Abies cephalonica*) and Aleppo Pine (*Pinus halepensis*) forests on the slopes beneath 1,000 m altitude, grasses and shrubs dominate above 1,000m, and under 300m farmlands dominate to the north with suburban housing to the east. The climate is continental, characterized by cold winters and warmer summers. Summer temperatures do not usually exceed 18°C, while in winter temperatures are frequently around 0°C, with an annual average of 11°C (Ganatsas *et al.,* 2012). Average rainfall in the area is 822 mm (at 1,000 m elevation), with approximately 70 rainy days per year.

In the summer of 2007, Greece was hit by the most devastating large fires in its recent history. Specifically on June 27th, 2007, a fire erupted in an area approximately 15 km west of the core of mount Parnitha National Park. On the next day, fanned by a medium strength west wind, it entered the forested western slopes and canyons of the mountain and spread to the summit leaving only charred trees. Its main run stopped when it reached sparse vegetation on the east slope of the mountain in the morning of June 29th. Fought by aerial fire-fighting support, it was controlled three days later (July 1st, 2007).


**[ Figure 1** *Location of our study area (shown in the red box)* **]**


## 3. Datasets

Multispectral imagery from the ASTER sensor acquired shortly after the fire suppression (acquisition date: July 20th, 2007) was the primary data source to satisfy the objectives of our study. ASTER is a satellite radiometer onboard the Terra polar orbiting platform, launched end of 1999. The sensor is capable of acquiring data at 15 spectral bands across the visible (VIS) to thermal infrared (TIR) parts of electromagnetic radiation spectrum at a spatial resolution varying from 15 to 90m. ASTER has numerous unique design features that make it in many respects rather superior to other similar instruments. These include increased multispectral coverage, higher spatial resolution in certain of the spectral bands, and a stereoscopic capability. These make the sensor an important tool particularly to conduct applications related to modelling land surface studies where heterogeneity and topography variations are important, including natural hazards such burnt area mapping Detailed information on the ASTER product can be found on the National Aeronautics and Space Administration (NASA) Jet Propulsion Laboratory website (http://asterweb.jpl.nasa.gov/documents.asp).

For this study, three operationally distributed products of the same post-fire image were obtained from the ASTER distribution centre in Japan. Those consisted of the registered radiance at the sensor (ASTL1B), the Surface Radiance (AST09) and the on-Demand Orthorectified (AST14OTH) image product. The ASTL1B is the registered radiance at the sensor product on which are co-registered the spectral bands from all the spectral channels of the sensor, and is radiometrically and geometrically corrected. It has been derived from the Level-1A data on which have been applied the radiometric calibration and geometric correction coefficients. Also, both intra-telescope and inter-telescope registration correction for all the bands has been performed relative to the reference band for each sub-system (i.e. Bands 2, 6, and 11)

(http://asterweb.jpl.nasa.gov/documents.asp). The AST1B dataset is provided in a single multi-file packaged either in .hdf or .geotiff format or at a Universal Transverse Mercator (UTM) projection. The AST09 product contains the atmospherically corrected VNIR and SWIR bands data. It is derived from the ASTER Level-1B image. Atmospheric correction involves deriving a relationship between the surface radiance/reflectance and the top of the atmosphere (TOA) radiance from information on the scattering and absorbing characteristics of the atmosphere. The product is provided in either .hdf or .geotiff format and at UTM projection. The AST14OTH product contains imagery transformed from a perspective projection to an orthogonal one. It is terrain-corrected and provides radiometrically calibrated radiance. It is computed using as inputs the ASTER L1A product, georeferencing information from the ASTER instrument's and Terra platform's ephemeris and attitude data and an ASTER-derived digital elevation model (DEM). The product includes fifteen orthorectified Level-1B calibrated radiance images, one per band and at a UTM projection in .geotiff format at original spatial resolution provided in the Level 1A product. More details on the different ASTER products can be found in Abrams *et al.*, (2002). In addition to the ASTER image products, a vector layer (shapefile format) of the burnt area was used, which was derived from manual digitisation of the burnt area based on direct photo-interpretation of the visible/near infrared bands (15 m) of the AST14OTH product. For all the different products included in our analysis the radiance image product was used to ensure consistency and comparability in our analysis. This dataset of the three ASTER image products formed the reference dataset used in our study against which the burnt area estimates from the different techniques were compared to, as described later on (section 4.3).

## 4. Methodology

An overview of the methodology followed in extracting the burnt area from the post-fire ASTER image products is illustrated in Figure 2. The remainder of this section provides an overview of the main pre-processing steps implemented. All pre-processing and geospatial analysis of the spatial datasets were carried out using ENVI (v. 5.0, ITT Visual Solutions), eCognition (v8) and ArcGIS (v. 10.1, ESRI) image analysis software platforms.

[ **Figure 2** *Overall methodology implemented in our study* ]

### 4.1 Pre-processing

The pre-processing of the ASTER images entailed a series of steps, depending on the product type (Figure 2). As ASTER spatial resolution varies from the VNIR (15m) to SWIR (30m), image resampling of the three VNIR ASTER bands was performed to match the spatial resolution of the SWIR bands, where appropriate. Image to image co-registration between the ASTER images and also the DEM was then performed to spatially co-register all data layers using the AST14OTH orthorectified image were used as a base image. A set of approximately 30 Ground Control Points (GCPs) randomly selected points clearly distinguishable on both the base and each of the other image products were used to perform the datasets co-registration. Image warping was performed by applying the nearest neighbour method, allowing a co-registration of all the images into a common UTM 34N projection under a WGS84 ellipsoid. To

check the co-registration accuracy, the coordinates of ~10 additional GCPs not previously included in the transformation were determined from the base image used. Results showed a positional accuracy within the sensor pixel range (i.e. < 30 m), which was considered satisfactory. Next, all the datasets were clipped to a smaller area covering an area that included the burn scar and sufficient ample land outside its perimeter.

## 4.2 Burnt Area Delineation

Burnt area was delineated from each of the ASTER pre-processed datasets using the ML and SVMs classifiers. The remainder of this section is focused in providing a brief explanation of the principles underlying the operation of each approach, including a description of the steps taken in extracting the burnt area from the ASTER pre-processed image from each technique.

### 4.2.1 Maximum Likelihood (ML)

ML implementation was performed using ENVI, following three main steps. First, a classification scheme was formulated, which consisted of the following classes: burned area, agricultural areas, urban fabric/bare soil areas, forests, and scrubland/vegetation areas. Decision to use those specific classes was assisted by our familiarity with the study area from previous work conducted in the same region (Petropoulos *et al.*, 2011; Petropoulos *et al.,* 2010b). Subsequently, training pixels were carefully selected from the AST14OTH image. The training sites were carefully determined based on the homogenous nature of pixels with respect to tone, texture, association, etc., within a similar class. Their selection was guided by photo-interpretation of a near concurrent to the ASTER Google Earth very high resolution imagery. Approximately 270 pixels of each class were identified as training data. For the selected training pixels it was examined their statistical separability in ENVI, by computing both the Jeffries-Matusita and the Transformed Divergence separability indices in (ENVI User Guide, 2008). A separability index for all class pairs was higher than 1.71 in all cases examined was reported which was considered as satisfactory. Then, the selected training points were used to parameterise the ML classifier and implement it in each of the ASTER products. A single threshold value for all classes in the classification was set up, using probability threshold value equal to zero, meaning that no pixels lower than this value are classified and also using as a data scale factor one. This deemed to be appropriate based on trial and errors performed using different parameterisation and then using the classification accuracy as measure to identify most suitable parameterisation. This is an approach employed often in optimisation of classifiers parameterisation (Petropoulos *et al.*, 2012a; Volpi *et al.*, 2013).

### 4.2.2 Support Vector Machines

SVMs are a non-linear and non-parametric large margin supervised classification scheme developed on the basis of Vapnik's structural risk minimisation principle (Vapnik, 1995) with no priori information on the underlying data distribution (Foody and Mathur, 2004). SVMs separates the samples of different classes by finding the separating hyperplane or decision surface related to maximal margin minimizing the hinge loss function (Boser, 1992) and maximizing the distance between the hyperplane and the nearest positive and negative training

example, called the margin. The aim of these hyperplane is to provide the best separation between the two classes in a multidimensional feature space reducing the generalization error which is inversely proportional to the margin. The higher dimensional kernel space is implicitly performed by applying a kernel function. The non-linear kernel functions such as Gaussian, RBF, polynomial in SVMs implicitly work linearly in a higher dimensional space, corresponding to a non-linear solution in the input space, where the data naturally resides. The use of the kernel function essentially allows the data points to be classified to spread in a way that allows the fitting of a linear hyperplane (Singh *et al.*, 2013). SVMs also introduce a cost parameter C to quantify the penalty of misclassification errors in order to handle non-separable classification problems.

Herein, SVMs was implemented in ENVI to each of the pre-processed ASTER images using the same set of training points selected in the ML classifier implementation. This allowed ensuring consistency and comparability in the burnt results obtained from the different classifiers. The RBF kernel was used for performing the pair-wise SVMs classification which is well tested by many researchers and has also already been shown good classification results (Petropoulos *et al.*, 2011; Srivastava *et al.*, 2012). The RBF kernel was parameterised based on performing a number of trials of parameters combinations and then using classification accuracy as a measure of quality. Such an approach has also been adopted in the past in analogous studies of SVMs implementation as well (Park and Sandberg, 1991; Petropoulos *et al.*, 2012b; Singh *et al.*, 2013). The $\gamma$ parameter was set to a value equal to the inverse of the number of the spectral bands of the imagery used each time SVMs was implemented. The penalty parameter, which controls the trade-off between allowing training errors and forcing rigid margins, was set in each SVMs equal to its maximum value (i.e. 100), indicating that we were interested to create the most accurate possible model. The pyramid parameter was set to a value of zero, since each image we wished to be processed at full resolution. Finally, a classification probability threshold of zero was also used, which meant that all image pixels forced to be classified into one of the classes of the classification scheme.


## 4.3 Accuracy Assessment

An evaluation of the classification accuracy of the thematic maps produced from the ASTER imagery, including the burnt area class, was performed by computing the error matrix statistics. In particular, the overall accuracy (OA), user's (UA), producer's (PA) accuracy and the Kappa (Kc) statistics were derived (Congalton and Green, 1999). For this purpose, an additional set of approximately 60 representative pixels for each class included in our classification scheme were also selected. Validation points were generally selected in homogeneous regions and away from the locations where the training points had been collected, ensuring non-overlap of pixels between the training data and validation sites. To ensure consistency in our comparisons, the same set of validation points were used in evaluating the accuracy of all the thematic maps produced from the implementation of the different classifiers to the different ASTER products.

In addition to the error matrix, the burnt area estimates from the different techniques were compared each against our reference burnt area which was derived from direct photo-interpretation of the ASTOTH image product, following Kontoes et al. (2009). In this approach, accuracy of the burnt area detection is expressed in terms of detected area efficiency (DAE),

skipped area rate (SBA, omission error) and false area rate (FBA, commission error). These accuracy figures are computed as follows:

$$Detected\ Area\ Efficiency = \frac{DBA}{DBA + SBA} \quad , \quad (8)$$

$$Skipped\ Area\ Rate = \frac{SBA}{DBA + SBA} \quad , \quad (9)$$

$$False\ Area\ Rate = \frac{FBA}{DBA + FBA} \quad , \quad (10)$$

In the above equations, DBA is the Detected Burnt Area (i.e. the common area between the generated burn scar polygon and the reference in-situ polygon), FBA is the False Burnt Area (i.e. the area included in the generated burn scar polygon but not in the reference in-situ polygon) and SBA is Skipped Burnt Area (the area included in the reference in-situ polygon but not in the generated burn scar polygon). As from the error matrix approach statistical parameters are computed on the basis of "reference" points which selected directly from the image, the Kontoes et al. (2009) method provides a complimentary view of the detection accuracy of the burnt area estimate regionally. This is because it allows the entire predicted burnt area estimate to be evaluated regionally against another "spatial reference", i.e. a dataset that represents the whole burnt area and not only by using selected points from that (or other) dataset. Use of their method has already been demonstrated not only in validation studies of burnt areas from different algorithms, but also of relevant operationally distributed products (Kontoes *et al.*, 2009; Petropoulos et al. 2012). In order to enable overlay and facilitate efficiency in the burnt area comparisons using the Kontoes et al. (2009) approach, each burnt area estimate from each ASTER product was extracted from the corresponding classification maps and was then exported as shapefile (.shp) to match the format of the "reference" burnt area derived from digitisation earlier during the pre-processing step. The evaluation of the accuracy of the burnt area detection by this approach was performed in ArcGIS software platform (ESRI Inc., v. 9.3.1). As a reference burnt area estimate, it was used a vector polygon generated through direct digitizing of the burned area from the ASTOTH image.

## 5. Results

### 5.1 Classification accuracy

Some of the land use land cover thematic maps produced from the implementation of the different classifiers to the three ASTER products are illustrated in Figure 3, with the burned area class shown in red. All the associated accuracy statistics to these maps derived from the error matrix computation are also summarised in Tables 1 and 2.

For the case of the ML classifier implementation on the ASTER image products, OA was always higher than 93% with a slight improvement when including the SWIR spectral bands to the orthorectified and the raw (L1b) ASTER image. The atmospheric correction and orthorectification applied to the ASTER raw image improved the OA from 95.38% to 97.53%

and 95.98% respectively when the shortwave bands were included. As seen in Table 1, the values of the Kc and the OA were always greater than 0.92. According to Table 1, the "burned area" class was generally well discriminated from the other classes using the ML classifier reporting constantly a very high PA and UA. In fact, all the PA and UA of this class were superior to 95%. However, the scrubland class always reported the lowest accuracy from all the classes in all cases of classification. Also, the highest improvement of the UA and PA of the "burned area" class was obtained in the case of the ASTER orthorectified and raw image when including all the ASTER visible near-infrared and shortwave spectral bands to the classification. As shown in Table 1 the ASTER atmospherically corrected image has shown the best result in terms of PA (100%) and UA (100%) of the burned area class in both cases of inclusion and exclusion of the SWIR bands. Also can be observed the orthorectification of the ASTER image improved only the PA of the "burned area" class passing from 95.31% to 100%. Elsewhere, when only the VNIR spectral bands were included, the PA and UA of "forest" and "bare soil" classes were improved in both cases of atmospheric correction and orthrectification, whereas in the case of SWIR band inclusion, only the atmospheric correction was reported to improve the PA and UA of the classification except for the UA of the "agriculture "class which decreased slightly from 100% to 98.28%.

**[ Figure 3** *Thematic maps from the ML classifier implementation to the ASTER raw image (a), the atmospherically corrected image (b) and the orthorectified image (c), using only the VNIR spectral bands (left) and the VNIR and SWIR spectral bands (right).* **]**

In terms of the SVMs performance (Table 1), only the atmospheric correction of the ASTER raw image reported improvement in the OA of the classification from 94.15% to 96.92% and 98.87% to 99.01% when including to the SVMs classification only the VNIR and all the VNIR and SWIR spectral bands respectively. In this case, Kc has shown the same trend and was always greater than 0.9 with significant improvement for the raw image passing from 0.92 to 0.98, followed by the atmospherically corrected image from 0.96 to 0.98 when all the SWIR and VNIR bands were included. Both OA and Kc have been improved by the inclusion of the SWIR bands to the classification process in all the scenarios studied, providing more accurate results than what was recorded for the ML classifier (Table 1). In general, high PA and UA were reported for all classes with a slight improvement of the "burned area" UA when including only the visible near-infrared bands to the ASTER orthorectified image (Table 1). Also, the PA and UA of the burned area class obtained in all the cases of the ASTER images were 100% when including the SWIR bands, meaning that all the collected validation points were found to belong to the same burned class and all the classified points as burned area can be expected to be burned area when a field survey is performed. Concerning the rest of the classes, except the PA of the forest class which improved from 98.38% to 100%, all the PA and UA accuracies of the classes decreased in the case of the orthorectified ASTER image. However, the results seem to suggest that neither the orthorectification nor the atmospheric correction improved the PA and UA accuracy of all the classes.

## 5.2 Spatial agreement of burned area estimates

The principal findings from the implementation of the Kontoes *et al.* (2009) accuracy assessment method from the implementation of ML classifier to the different ASTER image products are presented in Table 2. An initial inspection of the results makes apparent that the ASTER orthorectified image showed the best result compared with the two other images in terms of common burned area in cases of both exclusion and inclusion of the ASTER SWIR spectral bands (41.85 and 42.41 km$^2$ respectively). This result (Table 2) was followed by the atmospherically corrected image which has shown an improvement of the common burned area finding in both scenarios as well (40.96 and 40.64 km$^2$ respectively). Both orthorectification and atmospheric correction have demonstrated to decrease the false and skipped burned area (Table 2); the inclusion of all VNIR and SWIR ASTER bands to the SVMs implementation also decreased in the case of the atmospherically corrected image. Moreover, the false burned area was always smaller than the skipped in all cases of comparisons (Table 2). It is also interesting to note that the smallest absolute difference between the burned area retrieval and the validation dataset is observed in the case of the ASTER orthorectified image (5.95 km$^2$) when all the visible and SWIR ASTER bands are included in the classification. The above result was followed by the same image when only the ASTER visible spectral bands are included. These findings (Table 2) represent 12.3% and 13.5% respectively of the validation polygon used in the current study. Most of the skipped burned area is located along the borders of the extreme South-West and East side of Mt Parnitha region. The most accurate result in terms of absolute difference from the reference polygon is shown by the ASTER orthrectified image when SWIR bands were included (Figure 4).

The burnt area comparisons from the SVMs implementation to the ASTER products are illustrated in Figure 5 and the associated accuracy statistics are summarised in Table 2. An initial visual inspection of these maps also here shows a significant difference in terms of skipped and false burned area in some cases of scenarios implemented such as the inclusion of the ASTER SWIR bands to the SVMs developed model. As can be observed, the ASTER orthorectified image presented the closest prediction compared with the two other products in terms of common burned area in both cases of exclusion and inclusion of SWIR spectral bands (43.58 and 43.81 km$^2$ respectively). The ASTER atmospherically corrected image has also shown an improvement in the common burned area finding but only in the case of exclusion of SWIR bands (43.52 km$^2$). In terms of false and skipped burned area, the false burned area was always smaller than the skipped, and the orthorectified image achieved better improvement than the atmospherically corrected image (Table 2). Lastly, it is also interesting to note that the smallest absolute difference between the derived fire perimeter and the validation polygon is observed in the case of the orthorectified image (4.55 km$^2$) in the case of ASTER SWIR bands inclusion. The given area represented 9.4% of the reference validation polygon used in the present investigation

(Figure 6). This result is followed by those obtained from the atmospherically corrected (3.97 and 44.39 km$^2$) and raw (4.05 and 44.31 km$^2$) ASTER images. More recently, in an independent study Mondal et al. (2012) performed a comparative study of SVMs and ML applied to identify the accurate method for land use classification and they also reported in their study that accuracy was comparatively better in the SVMs method than the ML method.

[ **Table 2** *Surface accuracy assessment of the burnt area derived from the classifiers implemented to our ASTER products* ]

[ **Figure 5** *Thematic maps from the SVM classifier implementation to the ASTER raw image (a), the atmospherically corrected image (b) and the orthorectified image (c), using only the VNIR spectral bands (left) and the VNIR and SWIR spectral bands (right)* ]

[ **Figure 6** *Surface accuracy assessment maps from the SVM classifier implementation to the ASTER raw image (a), the atmospherically corrected image (b) and the orthorectified image (c), using only the VNIR spectral bands (left) and the VNIR and SWIR spectral bands (right)* ]

## 6. Discussion

Considering the error matrix of the accuracy assessment, the atmospherically corrected image showed evidently the best result in terms of OA and Kc in both ML and SVMs classifiers implementation. On the other hand, the general statistics (OA & Kc) produced from the SVMs classifier performance clearly outperformed those of the ML method with lowest performance in terms of OA, Kc, PA and UA. In fact, the inclusion of the three remaining SWIR ASTER bands to the classification process reported an improvement in the OA (between 1 and 4%) and Kc in all the three tested methods. The result can be explained by the fact that one of the direct consequences of fire is the loss of water by plant tissues (Busch and Smith, 1993). Therefore, this physiological change is easily detectable in the SWIR region of the ASTER sensor (1.6 - 2.43 µm) and of benefit for distinguishing between the healthy or unburned and burned vegetation. Furthermore, in a study over a site in Greece, Koutsias *et al.*, (2012) reported an increase in reflectance of burned surfaces observed in the middle-infrared region (2.08 - 2.35 µm or band 7) of the Landsat TM sensor which corresponds to ASTER 5, 6, 7 and 8 bands because of the water content. The improving incidence of ASTER SWIR band inclusion to the classification process was also reported in another study by Petropoulos *et al.*, (2012c), in which the authors concluded that the benefit from Advanced Land Imager (ALI) sensor use in burned area extraction appears to be partially due to its higher number of spectral SWIR bands.

Findings presented herein are also in close agreement to those reported by others who have explored the use of either the ML or the SVMs classifier in burn scar extraction from multispectral imagery. For example, Petropoulos et al. (2010a) combined ASTER and Landsat TM data respectively with the SVMs in mapping the extent of the burned area of the same fire event. The results presented herein outperformed the performance of the Artificial Neural Network (ANN) and Spectral Angle Mapper (SAM) classifiers when combined with the Landsat imagery reported to that study by the authors. More recently, Mallinis and Koutsias (2012) tested

the combination of ASTER data considering all the bands in the classification process of the ML for mapping fire scars in the Mt Parnitha 2007 fire. Results presented herein were comparable to the results from these authors for the ML implementation; yet even more accurate in the case of the atmospherically corrected image (97.53% of OA and 0.97 of Kc). Also, a close agreement has been reported herein with the results reported by Palandjian *et al.*, (2009), who assessed the post-fire impact in the Kassandra peninsula, Greece, using LANDSAT TM imagery and the ML classifier. In addition, many authors have reported some confusion occurring between the spectral signature of recently burned area and the shaded surfaces resulting from slope illumination and high topography variation, as is the case in many Mediterranean landscapes Pollet and Omi, 2002; Veraverbeke et al., 2010).

Koutsias *et al.*, (2012) conducted a study of the spectral signature of burned surfaces over the Mt Parnitha region and concluded that there was a strong decrease in the reflectance of burned surfaces observed in the near-infrared region (0.78-0.90 μm). As a general remark, a great spatial discontinuity of fire over the study area has been reported by all methods which mean small patches of unburned areas within the perimeter due to the topography and/or the vegetation response after fire. Additionally, a poor image co-registration could be at the origin of a spatial agreement problem when using the surface accuracy assessment method for evaluating the burned area. The origin of differences in terms of spatial distribution of burned area could be closely related to the land cover types of the study area and/or to the terrain structure. These two elements are the most important determining factors of burn severity in the Mediterranean region.


## 7. Conclusions

In the present study, the use of high resolution EO imagery was explored for mapping burnt scars from space using the Maximum Likelihood (ML), and Support Vector Machines (SVMs) image processing algorithms. In particular, this study was focused on investigating the potential added value of atmospheric correction, topographic correction and SWIR bands inclusion to the modelling of burnt area detection from space using these specific techniques using the techniques implemented in the ASTER global operational products. As a case study a fire event in a characteristic Mediterranean site was used for which post-fire ASTER imagery was available.

All the techniques used procured satisfactory results and provided clear evidence that the introduced methods offer advanced burned area mapping in terms of effectiveness and cost, compared to conventional field surveys. The SVMs classifier exhorted the best result in terms of overall accuracy, kappa coefficient and UA and PA of the "burned area" class. This at least appeared to be the case in this study. The ML was less accurate than SVMs, perhaps due to the high heterogeneity of vegetation on Mt Parnitha with respect to the fire behavioural spatial variability patterns which were difficult to be modelled adequately by either method.

The atmospheric correction applied to the ASTER raw image proved to bring a slight improvement. A more noticeable increase was exhorted by the orthorectified image in both cases of inclusion and exclusion of ASTER SWIR bands to the ML classifier. This means that the orthorectification step could be a necessary step to be included to any processing if the extent of burned area is to be mapped and there is high topography of the terrain. The inclusion of the

ASTER SWIR bands to the three ASTER image products also significantly improved the overall accuracy of classification. The combination of orthorectification and inclusion of SWIR bands to the ASTER raw image seems to an essential step prior to any method implementation procedure to accurately develop models in obtaining accurately burn area cartography from EO data.

The research indicates that an adaptive management are very much required in allowing fire and post fire hazard reduction projects to become successful. The final results of this study indicate the key steps that should be included in a methodology for burnt area mapping which would be potentially very beneficial for forest management and conservation officials. The same time, provides potentially very useful information towards the development of EO-based techniques that aim to operationally provide services related to the estimation of burnt area. This is of considerable scientific and practical value to the wider scientific and users' community, given the continuation of free access to resolution EO data from space globally.

## References
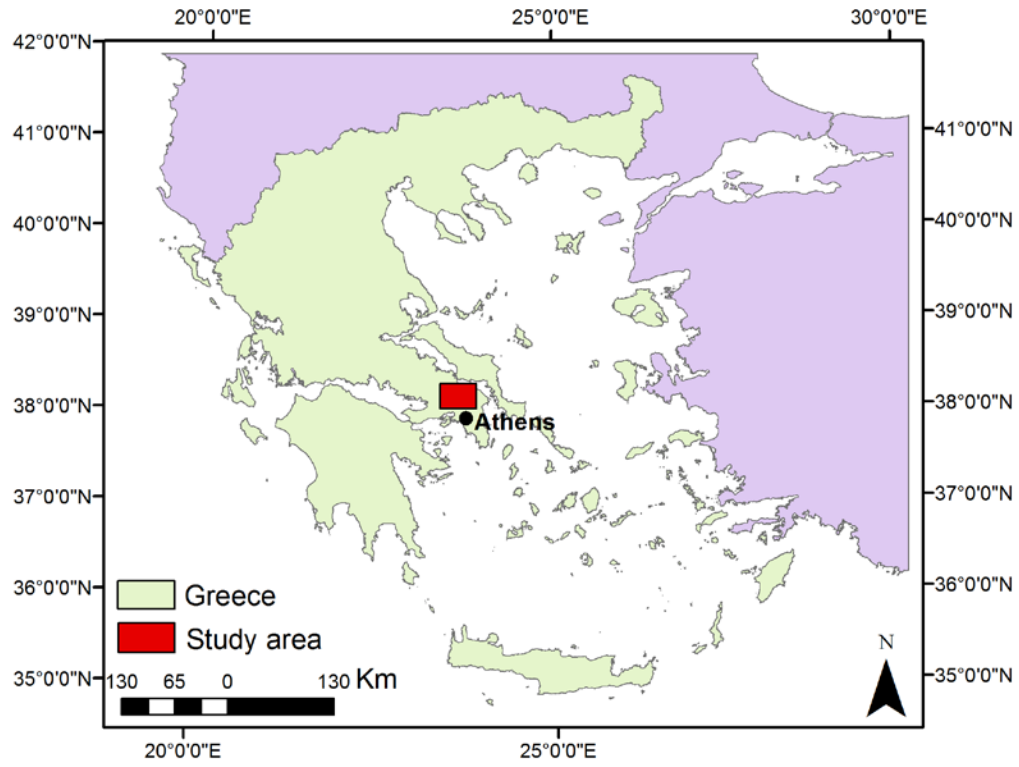
Abrams, M., Hook, S., Ramachandran, B., and Center, E. D.: ASTER User Handbook* Version 2, Jet Propulsion Laboratory, 4800, 2002.

Abrams, M. D. and Hulbert, L. C.: Effect of topographic position and fire on species composition in tallgrass prairie in northeast Kansas, American Midland Naturalist, 442-445, 1987.

Ahern, F. J., Goldammer, J. J. G., and Justice, C. O.: Global and regional vegetation fire monitoring from space: planning a coordinated international effort, Kugler Publications, 2001.

Banerjee, R. and Srivastava, P. K.: Reconstruction of contested landscape: Detecting land cover transformation hosting cultural heritage sites from Central India using remote sensing, Land Use Policy, 34, 193-203, 2013.

Bastarrika, A., Chuvieco, E., and Martín, M. P.: Mapping burned areas from Landsat TM/ETM+ data with a two-phase algorithm: Balancing omission and commission errors, Remote Sensing of Environment, 115, 1003-1012, 2011.

Boustras, G. and Boukas, N.: Forest fires' impact on tourism development: a comparative study of Greece and Cyprus, Management of Environmental Quality: An International Journal, 24, 498-511, 2013.

Busch, D. E. and Smith, S. D.: Effects of fire on water and salinity relations of riparian woody taxa, Oecologia, 94, 186-194, 1993.

Cao, X., Chen, J., Matsushita, B., Imura, H., and Wang, L.: An automatic method for burn scar mapping using support vector machines, International Journal of Remote Sensing, 30, 577-594, 2009.

Castillejo-González, I. L., López-Granados, F., García-Ferrer, A., Peña-Barragán, J. M., Jurado-Expósito, M., de la Orden, M. S., and González-Audicana, M.: Object-and pixel-based analysis for mapping crops and their agro-environmental associated measures using QuickBird imagery, Computers and Electronics in Agriculture, 68, 207-215, 2009.

Cawson, J. G., Sheridan, G. J., Smith, H. G., and Lane, P. N. J.: Effects of fire severity and burn patchiness on hillslope-scale surface runoff, erosion and hydrologic connectivity in a prescribed burn, Forest Ecology and Management, 310, 219-233, 2013

Chuvieco, E., Giglio, L., and Justice, C.: Global characterization of fire activity: toward defining fire regimes from Earth observation data, Global change biology, 14, 1488-1502, 2008.

Congalton, R. G.: Accuracy assessment and validation of remotely sensed and other spatial information, International Journal of Wildland Fire, 10, 321-328, 2001.

ENVI User Guide: ENVI on-line software user's manual, ITT Visual Information Solutions, 2008.

Foody, G. M., Campbell, N., Trodd, N., and Wood, T.: Derivation and applications of probabilistic measures of class membership from the maximum-likelihood classification, Photogrammetric Engineering and Remote Sensing, 58, 1335-1341, 1992.

Foody, G. M. and Mathur, A.: Toward intelligent training of supervised image classifications: directing training data acquisition for SVM classification, Remote Sensing of Environment, 93, 107-117, 2004.

Fuller, D. O.: Satellite remote sensing of biomass burning with optical and thermal sensors, Progress in Physical Geography, 24, 543-561, 2000.

Ganatsas, P., Daskalakou, E., and Paitaridou, D.: First results on early post-fire succession in an Abies cephalonica forest (Parnitha National Park, Greece), iForest-Biogeosciences and Forestry, 5, 6, 2012.

Giglio, L., Randerson, J., van der Werf, G., Kasibhatla, P., Collatz, G., Morton, D., and DeFries, R.: Assessing variability and long-term trends in burned area by merging multiple satellite fire products, Biogeosciences Discussions, 6, 2009.

Gitas, I. and Devereux, B.: The role of topographic correction in mapping recently burned Mediterranean forest areas from LANDSAT TM images, International Journal of Remote Sensing, 27, 41-54, 2006.

Hope, A., Albers, N., and Bart, R.: Characterizing post-fire recovery of fynbos vegetation in the Western Cape Region of South Africa using MODIS data, International Journal of Remote Sensing, 33(4), 979-999, 2012.

Huesca, M., Merino-de-Miguel, S., González-Alonso, F., Martínez, S., Miguel Cuevas, J., and Calle, A.: Using AHS hyper-spectral images to study forest vegetation recovery after a fire, International Journal of Remote Sensing, 34(11), 4025-4048, 2013.

Justice, C., Giglio, L., Korontzi, S., Owens, J., Morisette, J., Roy, D., Descloitres, J., Alleaume, S., Petitcolin, F., and Kaufman, Y.: The MODIS fire products, Remote Sensing of Environment, 83, 244-262, 2002.

Kasischke, E. S. and French, N. H.: Locating and estimating the areal extent of wildfires in Alaskan boreal forests using multiple-season AVHRR NDVI composite data, Remote Sensing of Environment, 51, 263-275, 1995.

Knorr, W., Pytharoulis, I., Petropoulos, G. P., and Gobron, N.: Combined use of weather forecasting and satellite remote sensing information for fire risk, fire and fire impact monitoring, Computational Ecology and Software, 1, 112-120, 2011.

Kontoes, C., Keramitsoglou, I., Papoutsis, I., Sifakis, N. I., and Xofis, P.: National scale operational mapping of burnt areas as a tool for the better understanding of contemporary wildfire patterns and regimes, Sensors, 13, 11146-11166, 2013.

Kontoes, C., Poilve, H., Florsch, G., Keramitsoglou, I., and Paralikidis, S.: A comparative analysis of a fixed thresholding vs. a classification tree approach for operational burn scar detection and mapping, International Journal of Applied Earth Observation and Geoinformation, 11, 299-316, 2009.

Koutsias, N., Arianoutsou, M., Kallimanis, A. S., Mallinis, G., Halley, J. M., and Dimopoulos, P.: Where did the fires burn in Peloponnisos, Greece the summer of 2007? Evidence for a synergy of fuel and weather, Agricultural and Forest Meteorology, 156, 41-53, 2012.

Koutsias, N., Karteris, M., and Chuvico, E.: The use of intensity-hue-saturation transformation of Landsat-5 Thematic Mapper data for burned land mapping, Photogrammetric Engineering and Remote Sensing, 66, 829-840, 2000.

Koutsias, N., Martínez-Fernández, J., and Allgöwer, B.: Do factors causing wildfires vary in space? Evidence from geographically weighted regression, GIScience & Remote Sensing, 47, 221-240, 2010.

Levin, N., Levental, S., and Morag, H.: The effect of wildfires on vegetation cover and dune activity in Australia's desert dunes: a multisensor analysis, International Journal of Wildland Fire, 21(4), 459-475, 2012.

Li, R. R., Kaufman, Y. J., Hao, W. M., Salmon, J. M., & Gao, B. C. (2004). A technique for detecting burn scars using MODIS data. Geoscience and Remote Sensing, IEEE Transactions on, 42(6), 1300-1308.

Lu, D. and Weng, Q.: A survey of image classification methods and techniques for improving classification performance, International Journal of Remote Sensing, 28, 823-870, 2007.

Mallinis, G., & Koutsias, N.: Comparing ten classification methods for burned area mapping in a Mediterranean environment using Landsat TM satellite data. International Journal of Remote Sensing, 33(14), 4408-4433, 2012.

Mondal, A., Kundu, S., Chandniha, S. K., Shukla, R., & Mishra, P. K.: Comparison of Support Vector Machine and Maximum Likelihood Classification Technique using Satellite Imagery, 2012.

NASA Jet Propulsion Labratory, 2004. *ASTER Documents.* [online] Available at: http://asterweb.jpl.nasa.gov/documents.asp [Accessed 5 June 2014].

Palandjian, D., Gitas, I. Z., and Wright, R.: Burned area mapping and post-fire impact assessment in the Kassandra peninsula (Greece) using Landsat TM and Quickbird data, Geocarto International, 24, 193-205, 2009.

Park, J. and Sandberg, I. W.: Universal approximation using radial-basis-function networks, Neural computation, 3, 246-257, 1991.

Patel, D., Gajjar, C., and Srivastava, P.: Prioritization of Malesari mini-watersheds through morphometric analysis: a remote sensing and GIS perspective, Environmental Earth Sciences, 69, 2643-2656, 2013.

Pérez-Cabello, F., de La Riva FernáNdez, J., Montorio Llovería, R., and García-Martín, A.: Mapping erosion-sensitive areas after wildfires using fieldwork, remote sensing, and geographic information systems techniques on a regional scale, Journal of Geophysical Research: Biogeosciences (2005–2012), 111, 2006.
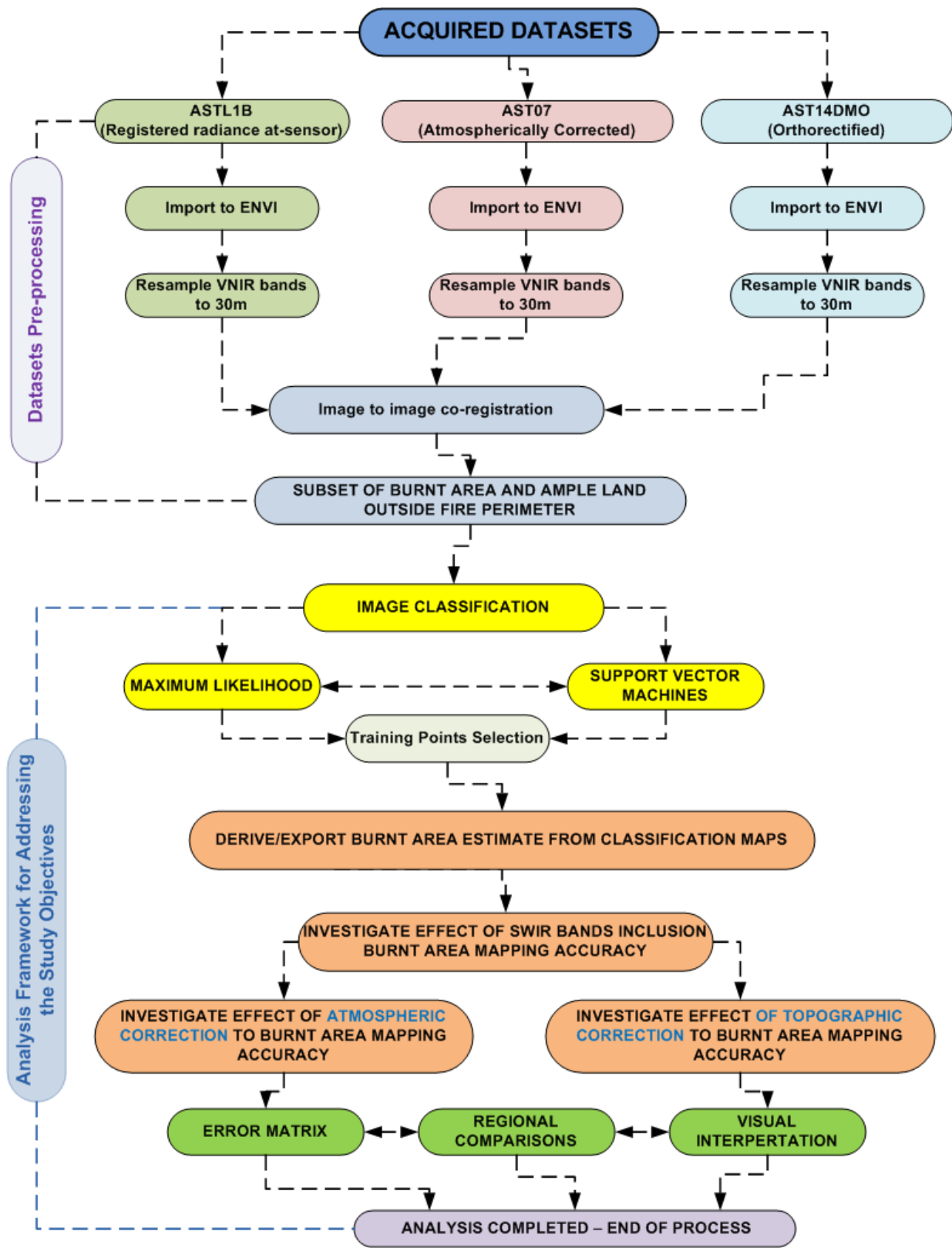
Petropoulos, G., Knorr, W., Scholze, M., Boschetti, L., and Karantounias, G.: Combining ASTER multispectral imagery analysis and support vector machines for rapid and cost-effective post-fire assessment: a case study from the Greek wildland fires of 2007, Natural Hazards and Earth System Science, 10, 305-317, 2010a.

Petropoulos, G. P., Arvanitis, K., and Sigrimis, N.: Hyperion hyperspectral imagery analysis combined with machine learning classifiers for land use/cover mapping, Expert systems with Applications, 39, 3800-3809, 2012a.

Petropoulos, G. P., Kalaitzidis, C., and Prasad Vadrevu, K.: Support vector machines and object-based classification for obtaining land-use/cover cartography from Hyperion hyperspectral imagery, Computers & Geosciences, 41, 99-107, 2012b.

Petropoulos, G. P., Kontoes, C., and Keramitsoglou, I.: Burnt area delineation from a uni-temporal perspective based on Landsat TM imagery classification using Support Vector Machines, International Journal of Applied Earth Observation and Geoinformation, 13, 70-80, 2011.

Petropoulos, G. P., Vadrevu, K. P., Xanthopoulos, G., Karantounias, G., and Scholze, M.: A comparison of spectral angle mapper and artificial neural network classifiers combined with Landsat TM imagery analysis for obtaining burnt area mapping, Sensors, 10, 1967-1985, 2010b.

Petropoulos, G.P., C. C. Kontoes &. Keramitsoglou (2012c): Land cover mapping with emphasis to burnt area delineation using co-orbital ALI and Landsat TM imagery. International Journal of Applied Earth Observation and Geoinformation, 18, 344-355

Pollet, J. and Omi, P. N.: Effect of thinning and prescribed burning on crown fire severity in ponderosa pine forests, International Journal of Wildland Fire, 11, 1-10, 2002.

Rothermel, R. C.: A mathematical model for predicting fire spread in wildland fuels, USFS, 1972.

Roy, D. P. and Boschetti, L.: Southern Africa validation of the MODIS, L3JRC, and GlobCarbon burned-area products, Geoscience and Remote Sensing, IEEE Transactions on, 47, 1032-1044, 2009.

Salvador, R., Lloret, F., Pons, X., and Pinol, J.: Does fire occurrence modify the probability of being burned again? A null hypothesis test from Mediterranean ecosystems in NE Spain, Ecological Modelling, 188, 461-469, 2005.

Schroeder, W., Ruminski, M., Csiszar, I., Giglio, L., Prins, E., Schmidt, C., and Morisette, J.: Validation analyses of an operational fire monitoring product: The Hazard Mapping System, International Journal of Remote Sensing, 29, 6059-6066, 2008.

Simon, M., Plummer, S., Fierens, F., Hoelzemann, J., and Arino, O.: Burnt area detection at global scale using ATSR-2: The GLOBSCAR products and their qualification, Journal of Geophysical Research: Atmospheres (1984–2012), 109, 2004.

Singh, S., Srivastava, P., Gupta, M., Thakur, J., and Mukherjee, S.: Appraisal of land use/land cover of mangrove forest ecosystem using support vector machine, Environmental Earth Sciences, 1-11, 2013.

Srivastava, P. K., Han, D., Ramirez, M. R., Bray, M., and Islam, T.: Selection of classification techniques for land use/land cover change investigation, Advances in Space Research, 2012.

Stroppiana, D., Grégoire, J.-M., and Pereira, J. M.: The use of SPOT VEGETATION data in a classification tree approach for burnt area mapping in Australian savanna, International Journal of Remote Sensing, 24, 2131-2151, 2003.

Tsela, P., Wessels, K., Botai, J., Archibald, S., Swanepoel, D., Steenkamp, K., and Frost, P.: Validation of the Two Standard MODIS Satellite Burned-Area Products and an Empirically-Derived Merged Product in South Africa, Remote sensing, 6, 1275-1293, 2014.

Turner, M. G., Hargrove, W. W., Gardner, R. H., and Romme, W. H.: Effects of fire on landscape heterogeneity in Yellowstone National Park, Wyoming, Journal of Vegetation Science, 5, 731-742, 1994.

Vafeidis, A. T., and Drake, N. A.: A two-step method for estimating the extent of burnt areas with the use of coarse-resolution data. International Journal of Remote Sensing, 26(11), 2441-2459, 2005.

Van Wagtendonk, J. W., Root, R. R., and Key, C. H.: Comparison of AVIRIS and Landsat ETM+ detection capabilities for burn severity, Remote Sensing of Environment, 92, 397-408, 2004.

Vapnik, V., Golowich, S. E., and Smola, A.: Support vector method for function approximation, regression estimation, and signal processing, Advances in neural information processing systems, 281-287, 1997.

Veraverbeke, S., Verstraeten, W. W., Lhermitte, S., & Goossens, R.: Illumination effects on the differed Normalized Burn Ratio's optimality for assessing fire severity. International Journal of Applied Earth Observation and Geoinformation, 12(1), 60-70, 2010.

Volpi, M., Petropoulos, G. P., and Kanevski, M.: Flooding extent cartography with Landsat TM imagery and regularized kernel Fisher's discriminant analysis, Computers & Geosciences, 2013.

**Figure 1** *Study area location (shown in the red box)*

1
2
3
4
5

ACQUIRED DATASETS

**Datasets Pre-processing**

ASTL1B
(Registered radiance at-sensor)

AST07
(Atmospherically Corrected)

AST14DMO
(Orthorectified)

Import to ENVI

Import to ENVI

Import to ENVI

Resample VNIR bands to 30m

Resample VNIR bands to 30m

Resample VNIR bands to 30m

Image to image co-registration

SUBSET OF BURNT AREA AND AMPLE LAND OUTSIDE FIRE PERIMETER

**Analysis Framework for Addressing the Study Objectives**

IMAGE CLASSIFICATION

MAXIMUM LIKELIHOOD

SUPPORT VECTOR MACHINES

Training Points Selection

DERIVE/EXPORT BURNT AREA ESTIMATE FROM CLASSIFICATION MAPS

INVESTIGATE EFFECT OF SWIR BANDS INCLUSION BURNT AREA MAPPING ACCURACY

INVESTIGATE EFFECT OF ATMOSPHERIC CORRECTION TO BURNT AREA MAPPING ACCURACY

INVESTIGATE EFFECT OF TOPOGRAPHIC CORRECTION TO BURNT AREA MAPPING ACCURACY

ERROR MATRIX

REGIONAL COMPARISONS

VISUAL INTERPERTATION

ANALYSIS COMPLETED – END OF PROCESS

1
2
3 **Figure 2** *Overview of the methodology implemented*
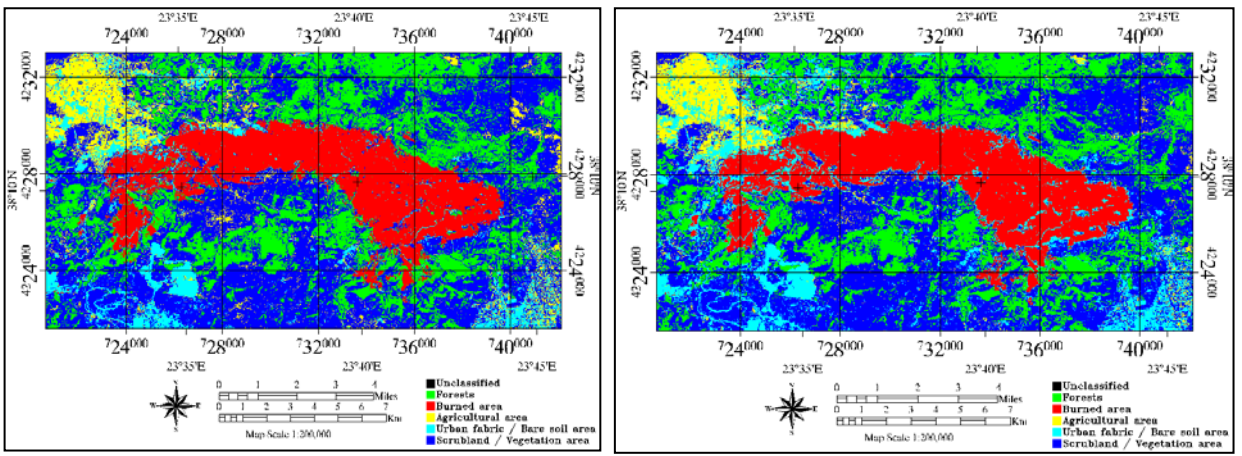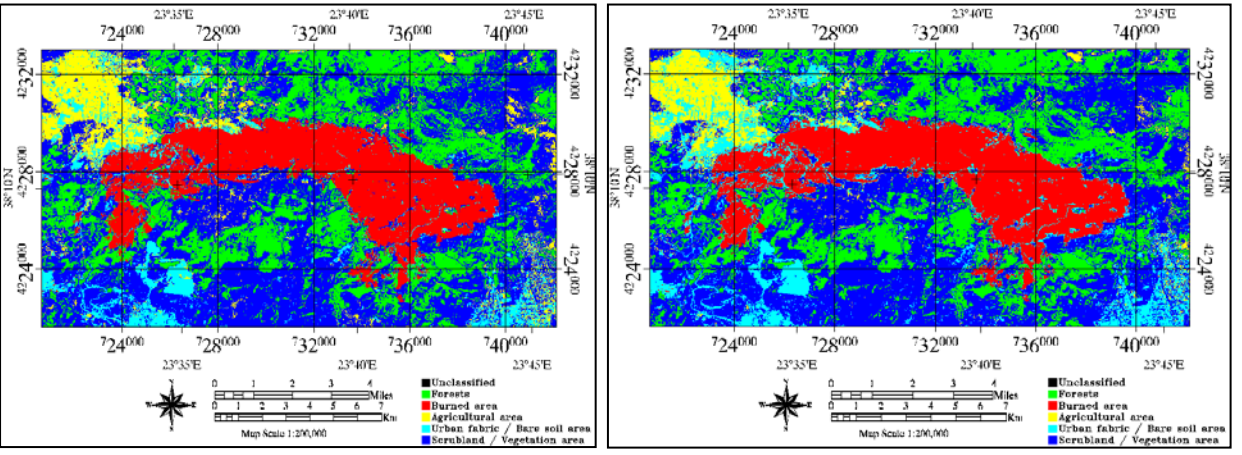
**Figure 3** *Thematic maps from the ML classifier implementation to the ASTER raw image (a), the atmospherically corrected image (b) and the orthorectified image (c), using only the VNIR spectral bands (left) and the VNIR and SWIR spectral bands (right).*

**Figure 4** *Surface accuracy assessment maps from the ML classifier implementation to the ASTER raw image (a), the atmospherically corrected image (b) and the orthorectified image (c), using only the VNIR spectral bands (left) and the VNIR and SWIR spectral bands (right)*
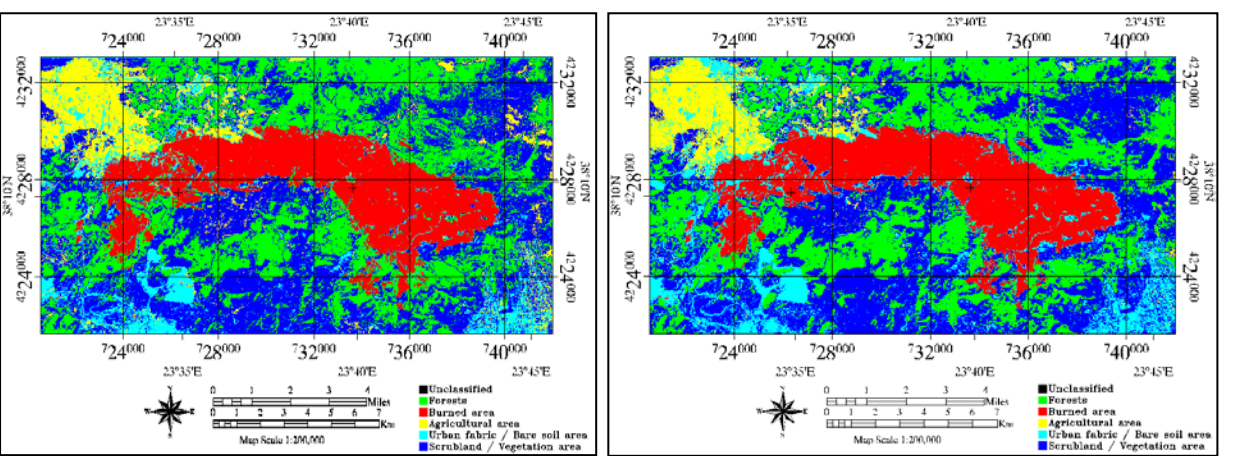
**Figure 5** *Thematic maps from the SVM classifier implementation to the ASTER raw image (a), the atmospherically corrected image (b) and the orthorectified image (c), using only the VNIR spectral bands (left) and the VNIR and SWIR spectral bands (right)*

**(a)**



**(b)**

**(c)**

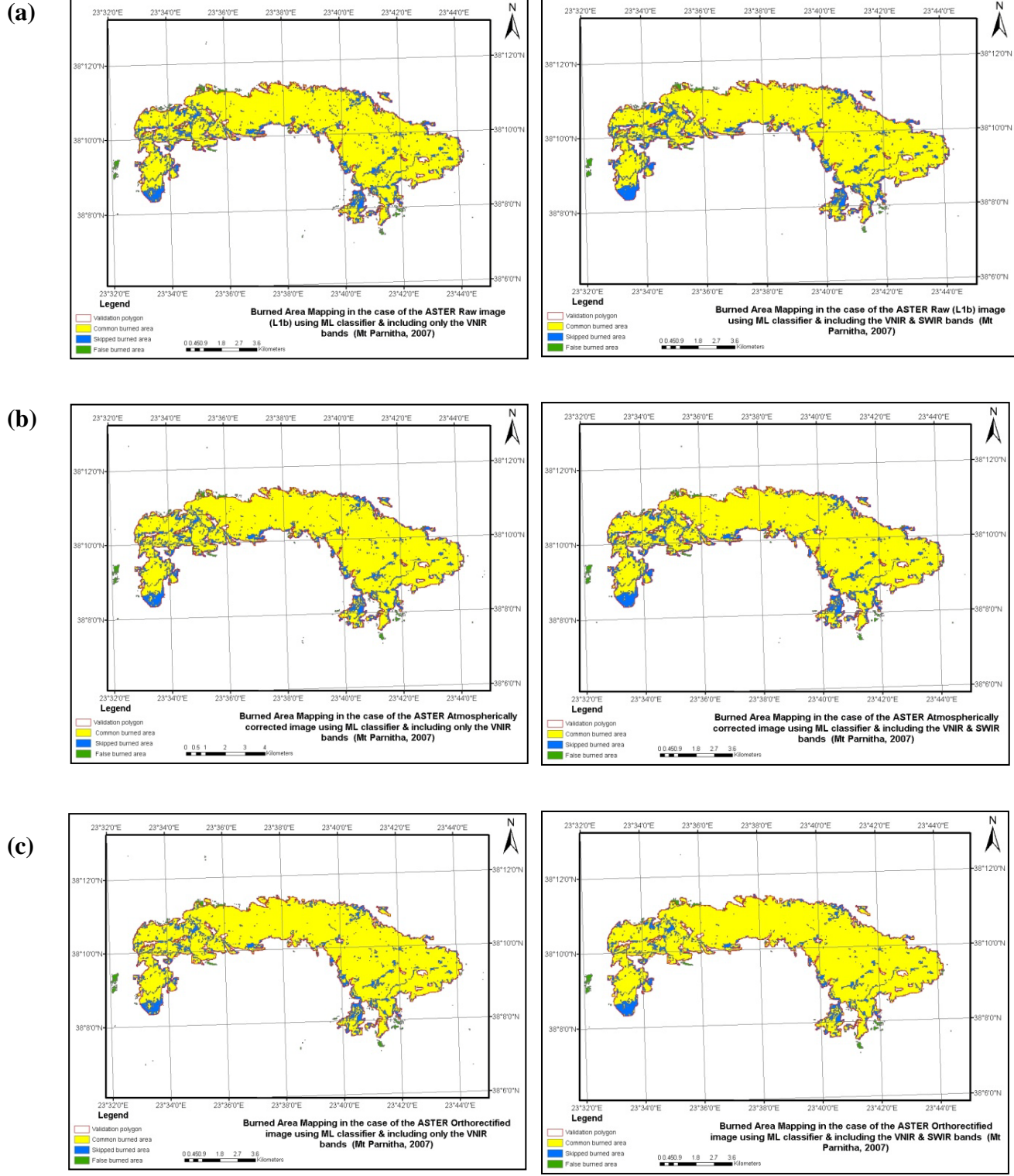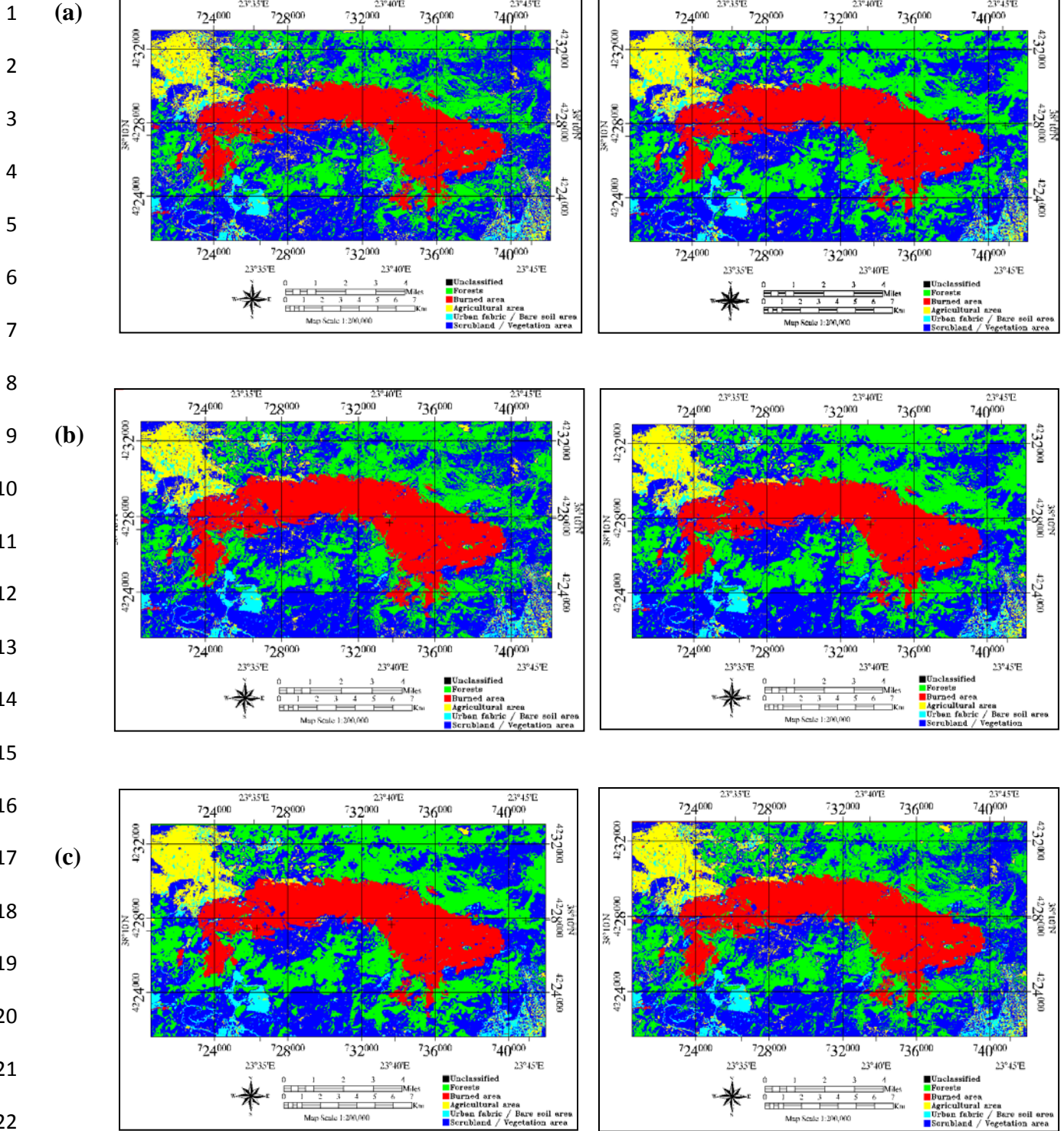**Figure 6** *Surface accuracy assessment maps from the SVM classifier implementation to the ASTER raw image (a), the atmospherically corrected image (b) and the orthorectified image (c), using only the VNIR spectral bands (left) and the VNIR and SWIR spectral bands (right).*
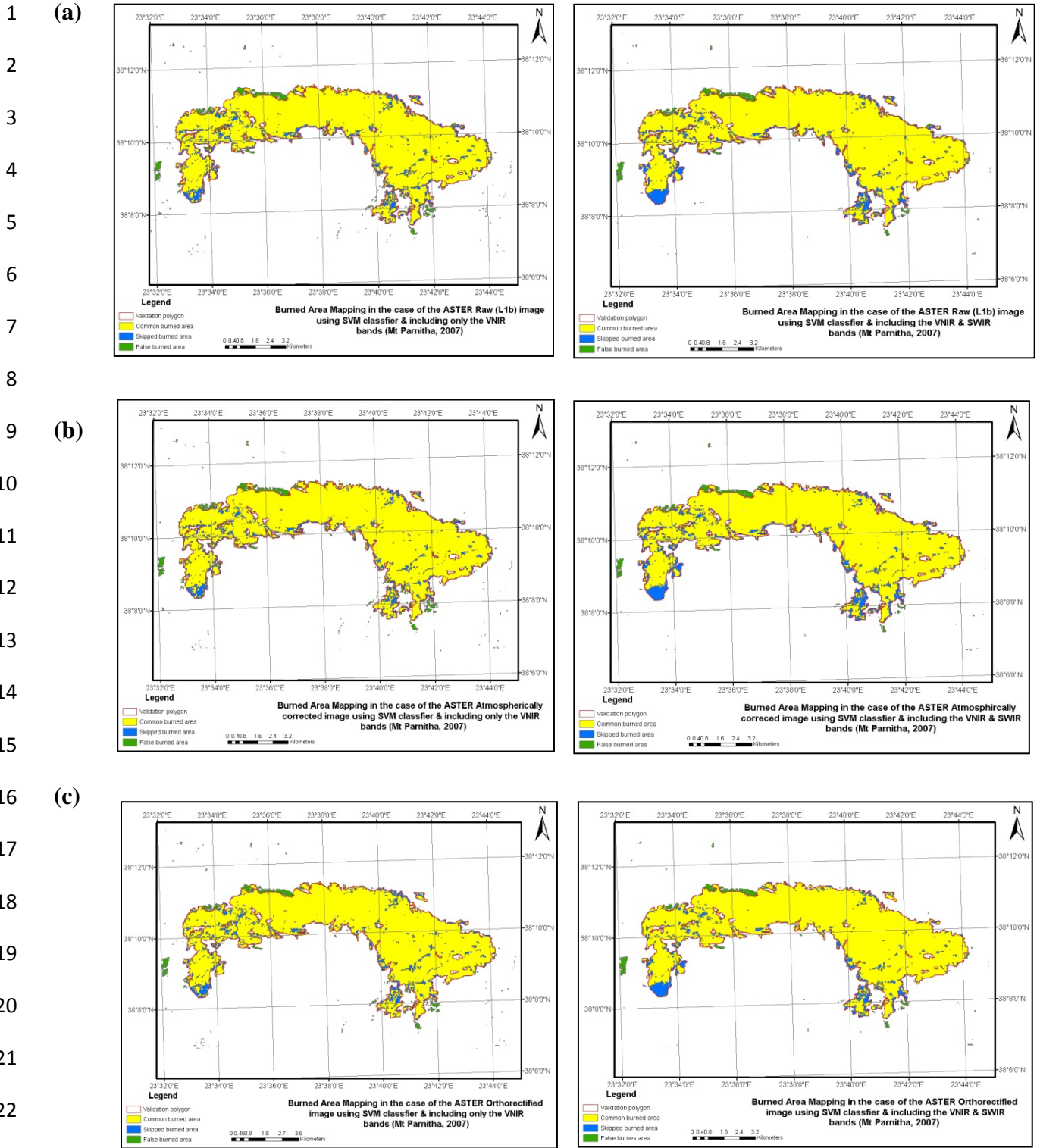
**Table 1** *Classification accuracy assessment results from the different scenarios implemented using a range of ASTER image products*

| Combination of spectral bands | ASTER Product | ML CLASSIFICATION | | | | | |
|---|---|---|---|---|---|---|---|
| | | Raw (L1b) | | Atmospherically corrected | | Orthorectified | |
| | Class | Producer's % | User's % | Producer's % | User's % | Producer's % | User's % |
| VNIR | Forest | 97.06 | 89.19 | 100 | 90.67 | 100 | 83.95 |
| | Burned area | 98.39 | 95.31 | 100 | 100 | 98.39 | 100 |
| | Bare soil | 94.74 | 100 | 100 | 100 | 97.37 | 98.67 |
| | Scrubland | 88.71 | 87.30 | 88.71 | 98.21 | 75.81 | 94 |
| | Agriculture | 91.23 | 100 | 98.25 | 100 | 96.43 | 94.74 |
| | **OA** | **94.15** | | **97.53** | | **93.82** | |
| | **Kappa** | **0.926** | | **0.969** | | **0.922** | |
| VNIR + SWIR | Forest | 100 | 87.18 | 100 | 90.67 | 100 | 95.77 |
| | Burned area | 100 | 100 | 100 | 100 | 98.39 | 100 |
| | Bare soil | 100 | 98.70 | 100 | 100 | 98.68 | 94.94 |
| | Scrubland | 82.26 | 92.73 | 87.10 | 100 | 90.32 | 93.33 |
| | Agriculture | 92.98 | 100 | 100 | 98.28 | 91.07 | 96.23 |
| | **OA** | **95.38** | | **97.53** | | **95.98** | |
| | **Kappa** | **0.942** | | **0.969** | | **0.949** | |

| Combination of spectral bands | ASTER Product | SVMs CLASSIFICATION | | | | | |
|---|---|---|---|---|---|---|---|
| | | Raw (L1b) | | Atmospherically corrected | | Orthorectified | |
| | Class | Producer's % | User's % | Producer's % | User's % | Producer's % | User's % |
| VNIR | Forest | 100 | 89.47 | 100 | 95.77 | 100 | 86.08 |
| | Burned area | 100 | 92.54 | 100 | 92.54 | 100 | 95.38 |
| | Bare soil | 92.11 | 100 | 92.11 | 100 | 89.47 | 100 |
| | Scrubland | 87.10 | 96.72 | 95.16 | 96.72 | 77.42 | 88.89 |
| | Agriculture | 91.23 | 100 | 98.25 | 100 | 96.43 | 93.10 |
| | **OA** | **94.15** | | **96.92** | | **92.59** | |
| | **Kappa** | **0.926** | | **0.961** | | **0.907** | |
| VNIR + SWIR | Forest | 98.38 | 98.06 | 98.06 | 98.06 | 100 | 89.47 |
| | Burned area | 100 | 100 | 100 | 100 | 100 | 100 |
| | Bare soil | 99.60 | 100 | 99.20 | 100 | 90.79 | 100 |
| | Scrubland | 97.99 | 96.70 | 97.99 | 97.34 | 93.55 | 95.08 |
| | Agriculture | 98.50 | 100 | 100 | 100 | 94.64 | 94.64 |
| | **OA** | **98.87** | | **99.01** | | **95.67** | |
| | **Kappa** | **0.986** | | **0.987** | | **0.945** | |

**Table 2** *Surface accuracy assessment of the burnt area detection from the scenarios implemented using different ASTER products. L1B-VNIR is the registered radiance at the sensor visible and near infrared bands only, Atmo-VNIR is the atmospherically corrected visible and near infrared bands only, Ortho-VNIR is the Orthorectified visible and near infrared bands only, VNIR+SWIR is used to indicate that all visible, near infrared and shortwave infrared bands have been used.*

### ML CLASSIFICATION

| Image code | Total BA (km²) | Common BA (km²) | False BA (km²) | Skipped BA (km²) | Detection efficiency rate | Commission error | Omission error |
|---|---|---|---|---|---|---|---|
| L1B-VNIR | 41.66 | 40.25 | 1.41 | 8.1 | 0.832 | 0.034 | 0.168 |
| Atmo-VNIR | 42.33 | 40.96 | 1.36 | 7.39 | 0.847 | 0.032 | 0.153 |
| Ortho-VNIR | 42.9 | 41.85 | 1.04 | 6.5 | 0.866 | 0.024 | 0.134 |
| L1B-VNIR+SWIR | 41.29 | 40.13 | 1.15 | 8.22 | 0.830 | 0.028 | 0.170 |
| Atmo-VNIR+SWIR | 41.83 | 40.64 | 1.18 | 7.71 | 0.841 | 0.028 | 0.159 |
| Ortho-VNIR+SWIR | 43.36 | 42.41 | 0.94 | 5.94 | 0.877 | 0.022 | 0.123 |

### SVMs CLASSIFICATION

| Image code | Total BA (km²) | Common BA (km²) | False BA (km²) | Skipped BA (km²) | Detection efficiency rate | Commission error | Omission error |
|---|---|---|---|---|---|---|---|
| L1B-VNIR | 45.73 | 43.1 | 2.63 | 5.26 | 0.891 | 0.058 | 0.109 |
| Atmo-VNIR | 46.26 | 43.52 | 2.73 | 4.83 | 0.900 | 0.059 | 0.100 |
| Ortho-VNIR | 45.66 | 43.58 | 2.08 | 4.77 | 0.901 | 0.046 | 0.099 |
| L1B-VNIR+SWIR | 45.01 | 42.93 | 2.07 | 5.42 | 0.888 | 0.046 | 0.112 |
| Atmo-VNIR+SWIR | 44.45 | 42.48 | 1.96 | 5.88 | 0.878 | 0.044 | 0.122 |
| Ortho-VNIR+SWIR | 45.54 | 43.81 | 1.73 | 4.54 | 0.906 | 0.038 | 0.094 |